AIAA SciTech Forum
9 - 13 January 2017, Grapevine, Texas
55th AIAA Aerospace Sciences Meeting

Boundary-Layer Transition Measurements in the Boeing/AFOSR Mach-6 Quiet Tunnel

Kathryn A. Gray*, Brandon C. Chynoweth*, Joshua B. Edelman*,
Gregory R. McKiernan*, Mark P. Wason*, and Steven P. Schneider†
School of Aeronautics and Astronautics
Purdue University
West Lafayette, IN 47907-1282

Recent results from several projects in the BAM6QT are presented. An infrared camera system was used to image a circular cone at an angle of attack, and the results are compared to previous TSP measurements. The IR images show clear streaks and demonstrate repeatability and low noise levels compared to TSP. Oil flow and surface pressure sensor measurements are presented for a cone with a slice and ramp. Separation and reattachment are discussed, along with the amplification and dampening of instabilities at various locations on the model. The temperature distribution along the BAM6QT nozzle wall was varied to study the relationship between heating and the percentage of a run which was quiet. No apparent correlation was observed. Pitot-probe measurements were taken at various locations on the nozzle centerline to investigate an increase in noise levels that occurs roughly two seconds into runs. The magnitude of the increase and the time at which it started depended on the Reynolds number. Development of higher-Reynolds number hypersonic quiet tunnel facilities may require the use of suction on the nozzle wall. Initial computations are presented for the design of a flared inlet centerbody that can be tested in the Boeing AFOSR/Mach-6 Quiet tunnel to determine the feasibility of creating sufficiently uniform suction. A stability analysis is performed to determine the most unstable second-mode frequencies and to compute the Görtler numbers on the flared aft-body portion. Finally, the 3 inch shock tube used for PCB calibration has been upgraded with high accuracy sensors and an automated pressure control system.

Nomenclature

Re_∞	unit Reynolds number
P_{0i}	initial stagnation pressure
t	time
z	distance from tunnel throat
M_∞	freestream Mach number
P_0	stagnation pressure
T_0	stagnation temperature
T_∞	freestream temperature
ρ_∞	frestream density
T_{wall}	wall temperature
G	Görtler number
Re_θ	Reynolds number based on momentum thickness
θ	momentum thickness
δ	boundary-layer thickness
f	second-mode frequency
v_e	edge velocity

Abbreviations

BAM6QT	Boeing/AFOSR Mach-6 Quiet Tunnel
TSP	Temperature-Sensitive Paint
PSD	Power-Spectral Density

*Research Assistant. Student Member, AIAA
†Professor. Associate Fellow, AIAA

I. Introduction

A. Hypersonic Boundary Layer Transition

An accurate understanding of boundary-layer transition is vital to the design of hypersonic vehicles because the state of the boundary layer directly affects the vehicle's aerodynamics and heating loads. However, the mechanisms of high-speed boundary-layer transition are not well understood. An important tool in understanding the processes of transition is the quiet tunnel. Quiet tunnels produce freestream noise around 0.05% or less, allowing the study of boundary-layer transition in a flight-like noise environment. Conventional wind tunnels have freestream noise levels orders of magnitude greater than those of flight. High freestream noise levels can cause early transition, or even change the responsible mechanisms.

B. The Boeing/AFOSR Mach-6 Quiet Tunnel

The Boeing/AFOSR Mach-6 Quiet Tunnel (BAM6QT) is one of three hypersonic quiet tunnels in the world. A schematic of the BAM6QT is provided in Figure 1. The BAM6QT is a Ludwieg tube composed of a long driver tube, a converging-diverging nozzle, and a large vacuum tank. Prior to a run, pressure in the driver tube is increased to the desired value while the sections downstream of the diaphragm are pumped to near-vacuum. When the diaphragms burst, a shock propagates downstream into the vacuum tank and an expansion fan propagates upstream through through the nozzle, starting the wind tunnel. The expansion fan reflects between the two ends of the driver tube, causing a stagnation pressure drop of about 1% per reflection. Each cycle lasts about 200 ms, during which the stagnation pressure is quasi-constant.

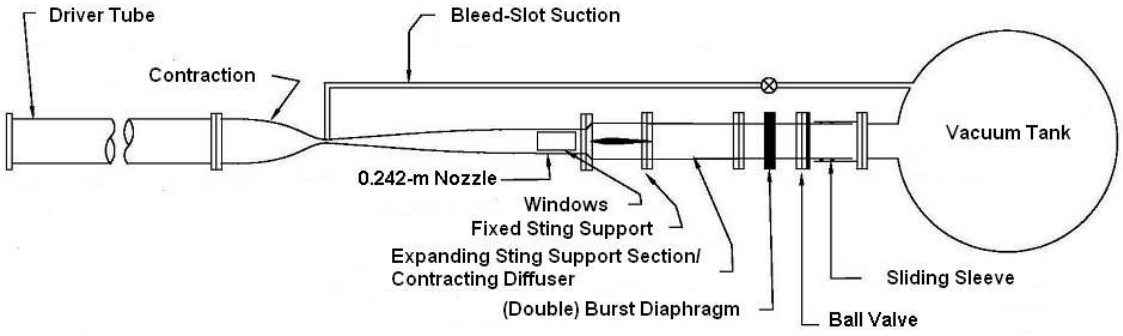

Figure 1. A schematic of the Boeing/AFOSR Mach-6 Quiet Tunnel.

The BAM6QT has several design features which keep the boundary layer laminar on the nozzle walls. The nozzle expansion section is polished to a mirror finish, and is very long to reduce the growth of the Görtler instability. Also, the air is filtered to minimize particulates. Finally, the boundary layer in the contraction is removed through a bleed slot just before the throat, enabling a fresh laminar boundary layer to form in the nozzle expansion. With these bleed valves open, the BAM6QT can run at unit Reynolds numbers up to 12.7×10^6 /m with freestream noise levels around 0.05% or lower. If the bleed slot at the throat is not used, the BAM6QT can be run as a conventional tunnel with noise levels near 3%.

II. Infrared Thermographic Measurements of a Pitched Cone

A 7° half-angle polyether ether ketone (PEEK) conical insert was fabricated for the Modular cone, previously used in a number of crossflow experiments in the BAM6QT.[1] PEEK has been used successfully in the BAM6QT for IR thermography of crossflow on an elliptic cone.[2] A specially-made calcium fluoride (CaF) window, provided by AFRL, was installed in the BAM6QT for IR optical access. This window is circular with a diameter of about 3 inches. With a wide-angle lens, the window is large enough to image the PEEK section of the Modular cone, but future experiments may require a larger window.

A. IR Camera

An Infratec ImageIR 8300 hp camera was used to image the PEEK. The camera was provided by the University of Notre Dame. According to the manufacturer the camera has a temperature resolution of 0.02 K and an accuracy of ±1° C. The sensor has a 640 x 512 resolution. For the present experiment, images were generally taken at 50 Hz.

A wide-angle 12 mm lens was used, which introduces significant distortion in the image. A basic algorithm to correct for distortion was implemented and the parameters were varied until the edges of the cone were straight lines in the corrected image.

B. Results

The Modular cone with the PEEK insert was run at 6° angle of attack with a sharp nosetip and a dimpled-Torlon roughness insert. This roughness insert has a wavenumber of 50 per circumference; more information on the roughness can be found in Edelman.[1] The PEEK insert has room for 24 PCB high-frequency pressure transducers, but for the present data these sensors were rotated out of view.

Figure 2(a) shows a distortion-corrected image from the IR camera. The 135° ray is centered in the view. This image is actually the difference between two images: an image during the run, and a pre-run image to measure to the initial temperature profile of the PEEK. The color scale is the temperature change from this pre-run state. Several streaks are immediately obvious in the IR image. From the temperature rise and subsequent broadening of the streaks, it appears that transition has occurred forward near the lee ray (but not on it), and aft closer to the 135° ray. The temperature-change image has been unwrapped in Figure 2(b), showing the axial-azimuthal map of the temperature change. There appear to be about 9 waves in the region from 100°-170°, giving a circumferential wavenumber of about 46 stationary vortices over the entire azimuth of the cone. This is in the range of the most unstable stationary wavenumber according to Li, et al.[3] It is also slightly less than the forced wavenumber of 50.

The repeatability of the PEEK-IR system is important to establish, especially in comparison to temperature-sensitive paint, or TSP, which is used in a number of experiments at Purdue University.[4] Figure 3 shows azimuthal cuts of the measured temperature change using both measurement techniques. Both of these measurements used the Modular cone, so only a 5.5 inch long Sensor Frustum near the base of the cone was different for each experiment. For the TSP measurements, the Sensor Frustum was aluminum, with the TSP painted on top. For the IR measurements, the Sensor Frustum was PEEK. The same roughness insert was used for both experiments, but its location may be slightly different in each. More information on the TSP measurements can be found in Edelman.[1] Note that the TSP measurements were made at a lower unit Reynolds number than the IR measurements. There has been no averaging performed on the raw camera data for either case.

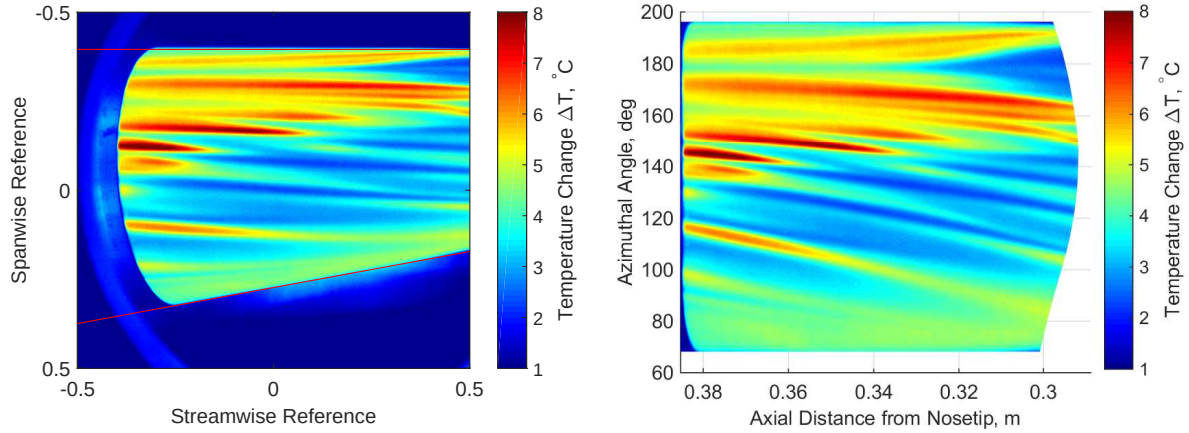

(a) Distortion-corrected image from IR camera. Color scale is temperature change from pre-run state. $Re_\infty = 12.2 \times 10^6$ /m.

(b) Axial-azimuthal unwrapped version of (a).

Figure 2. IR image from one run with the PEEK cone.

Figure 3(a) shows an azimuthal cut of the TSP at $x = 0.364$ m from the nosetip. There is significant noise, especially evident between 80°-115° and 120°-138°. In general, the peaks in the temperature change (associated with the thin boundary layer in the trough between stationary vortices) have repeatable amplitudes and locations. However, the high noise makes finding the 'true' peak locations difficult, and completely obscures any low-amplitude streaks.

Figure 3(b) shows an azimuthal cut of the IR data at $x = 0.360$ m from the nosetip. It is clear that the noise level is much lower in the IR than in the TSP. Streak location and amplitude repeatability is as good or better than the TSP. The streak at about 135° has a peak location difference of about 2° between the two runs. In addition, small streaks at 90° and 120° are evident in the IR, while they are obscured by noise in the TSP.

From these results, IR thermography seems to be a promising technique to complement surface-pressure measurements in the BAM6QT. Future crossflow research will continue to use the PEEK model, and will compare the measured growth of stationary crossflow waves using several methods, including IR. However, there is still a great deal of work left to do on the IR system. A method to infer heat transfer from the IR data is being developed. In addition, reliable access to a camera system will need to be solidified. Additional plans include possibly creating a larger CaF window.

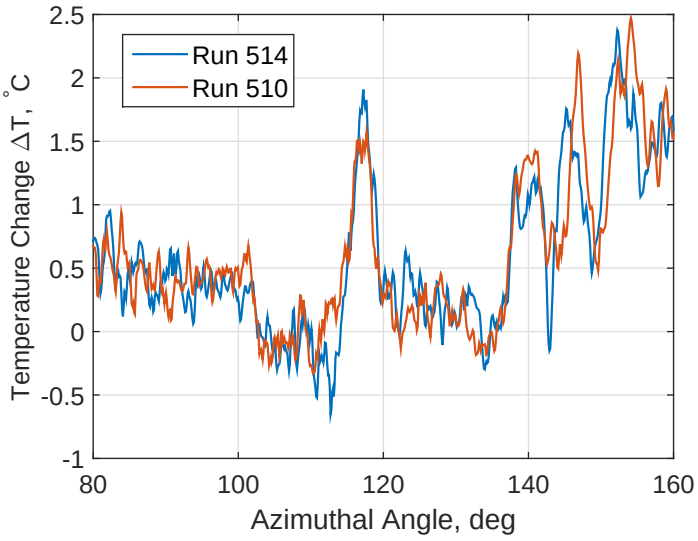

(a) TSP repeatability. $x = 0.364$ m, $Re_\infty = 10.9 \times 10^6$ /m.

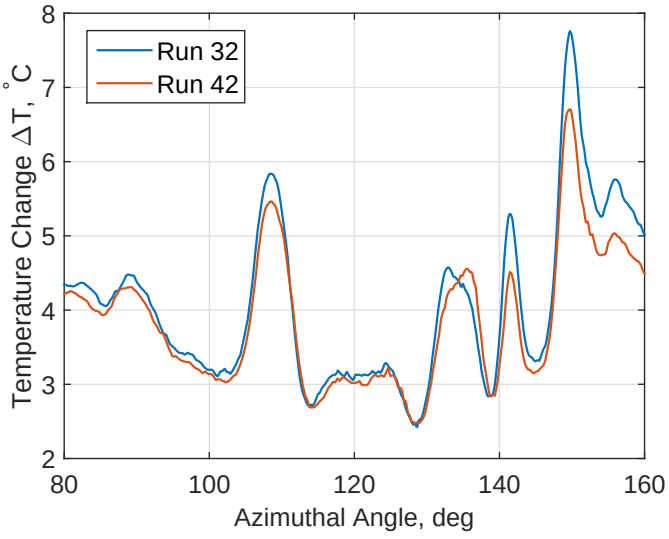

(b) IR repeatability. $x = 0.360$ m, $Re_\infty = 12.2 \times 10^6$ /m.

Figure 3. Comparison of thermographic repeatability between TSP and IR.

III. Transition measurements through a finite span compression corner

Boundary-layer flow approaching any ramp or control surface on a hypersonic vehicle is subjected to adverse pressure gradients due to the shock wave present at a compression corner. This adverse pressure gradient will retard the incoming boundary layer and, if strong enough, cause separation. At these locations, laminar-turbulent transition commonly occurs within the free-shear layer and can lead to some of the highest heating loads on the surface.[5] Gaining a basic understanding of how the free-shear layer affects the natural transition on a body will help in designing many maneuverable high speed vehicles.

A. Model

A variation of the model used by Oberkampf et. al. was designed and fabricated for use within the BAM6QT.[6] The model consists of a 7° half angle cone with a nominally sharp nose tip. At 0.7L, where L is the length of the model, a slice was machined into the cone. This slice is parallel with the model's axis and provides the surface upstream of the compression corner. Three interchangeable ramps are 0.038m long and allow deflection angles of 10°, 20°, and 30°. These ramps span the width of the slice.

Nine holes for PCB132A31 fast pressure sensors are on the surface of the model. Six of these are located on the slice and the last three were located on the ramp. Four PCB's were placed around the azimuth upstream of the slice to ensure the tests were conducted at 0.00° angle of attack. A schematic of the model can be seen in Figure 4 and an image in 5.

Previous measurements with PCBs and TSP did not provide a good picture of the flow field near and within the separation. As a result, another set of experiments was completed to obtain oil flow images. The colored oil consisted of DayGlo Color Aurora Pink pigment and 200 Centistokes Dow Corning Fluid. Quantities of the two ingredients were varied until the highest contrast image was acquired. The oil was applied to the surface and allowed to drip until all excess had fallen off the model.

The two blue LEDs used for TSP were also used to illuminate the oil. Additionally, the TSP camera was used to measure the intensity levels of the illuminated oil. Locations where the surface shear stress deposited large quantities of oil registered as larger intensities on the camera. Images were captured at 10 Hz with an exposure time of 20 ms. All images were 2x2 binned in order to improve the signal clarity and strength. No formal post-processing procedure has been successfully developed for oil flow images within the BAM6QT at this time.

Comprehending the surface flow field using oil flow images is not trivial. For the current results, the separation was interpreted as a region of low oil accumulation near the ramp corner with accumulation in an upstream arc at the separation point. Reattachment has a similar pattern.

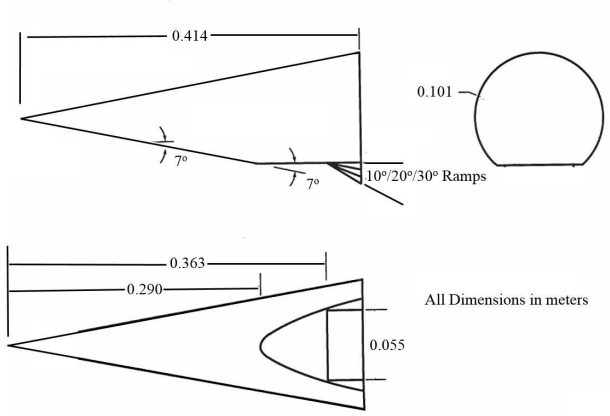

Figure 4. Schematic of the model with dimensions in meters. Redrawn from Reference [6]

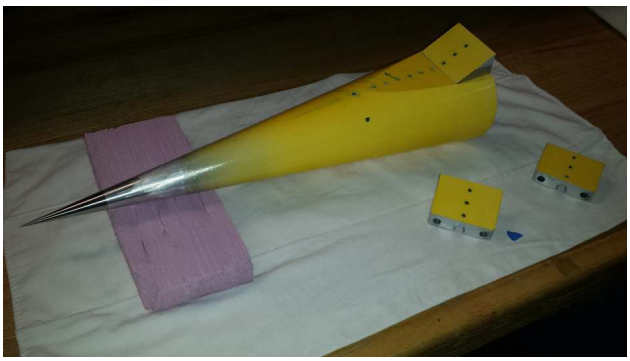

Figure 5. Photo of the model with TSP applied.

B. Current Results

Figures 6, 7, and 8 show the raw intensities picked up by the camera at various ramp angles in quiet and noisy flow for unit Reynolds numbers near the maximum for quiet flow in the BAM6QT.

Figure 6 shows the raw oil flow images for flow over the slice and 10° ramp. For the noisy flow image, the shear stress on the ramp is too large for the oils to remain on the surface. This was tested with several viscosities and none of the available oil could withstand noisy flow on the ramp surface. However, oil did remain on the slice surface, so the images are included in this section. Under quiet conditions, no separation can be seen in the 10° ramp images. Additionally, no evidence of reattachment is present in this case. It is possible that the separation is not large enough to be seen.

Figure 7 shows images of the oil in similar conditions for the 20° ramp. For quiet flow the oil shows a thin line of accumulated oil on the slice, close to the ramp. A possible reattachment stretches the streamwise and spanwise extent of the ramp. Noisy flow shows vortex-like structures near the ramp on the slice. The cause of these are unknown, although they could be due to the 3-dimensionality of the model.

Figure 8 shows similar images for the 30° ramp. For the quiet flow case the separation point appears to have moved further upstream while the possible downstream reattachment has shrunk on the ramp. In noisy flow the large vortex-like structures have grown and extend further upstream.

A comparison of these oil flow images with the PCB power spectra was made in order to help present a picture of surface pressure fluctuation development. Figure 9 show the PSD development at different axial distances downstream of the nosetip at varying Reynolds numbers. All of these figures correspond to the 20° ramp. The three furthest upstream sensors correspond to locations on the slice, while the three downstream sensors correspond to locations on the ramp. Figure 9(a) shows that an instability near the second mode frequency exists and matches with the pre-slice sensor spectra. At 0.332m and 0.370m downstream this instability damps and lower frequency peaks near 100-125 kHz grow. The expansion onto the flat slice seems to damp the second mode instability growth within the boundary layer. Figures 9(d) and 9(e) show ramp sensors and the instabilities have broadened in frequency and begun to grow. At the furthest downstream location the instability content begins to become obscured by a rising noise floor. This is indicative of transition but it has not developed enough for exact determination. Based on the previous oil flow images this coincides with the accumulation of oil on the ramp that is a possible reattachment. If the ramp was longer a better measurement of the post-reattachment boundary could be made.

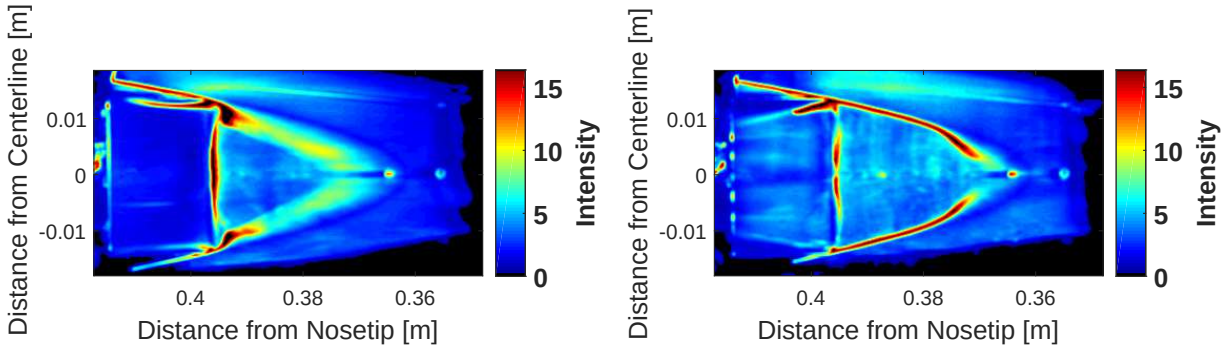

Figure 6. Oil flow on the model with 10° ramp. Left: Re = 11.8×10^6/m in noisy flow. Right: Re = 11.6×10^6/m in quiet flow.

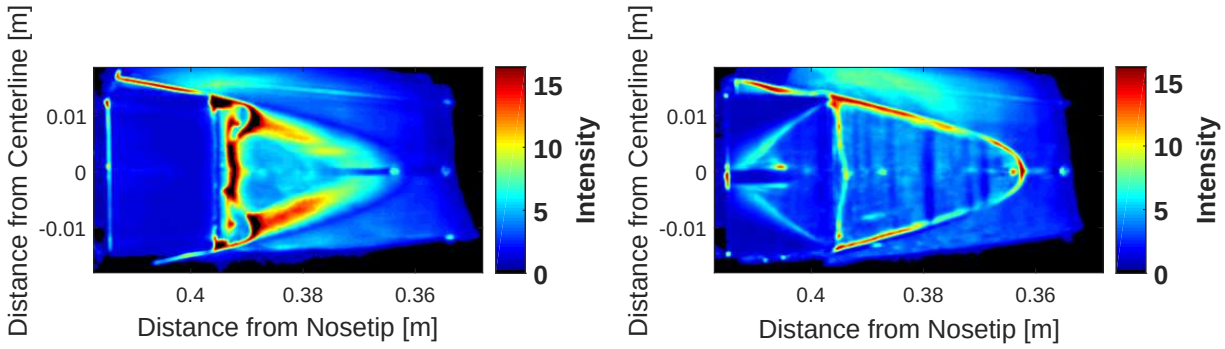

Figure 7. Oil flow on the model with 20° ramp. Left: Re = 11.6×10^6/m in noisy flow. Right: Re = 11.1×10^6/m in quiet flow.

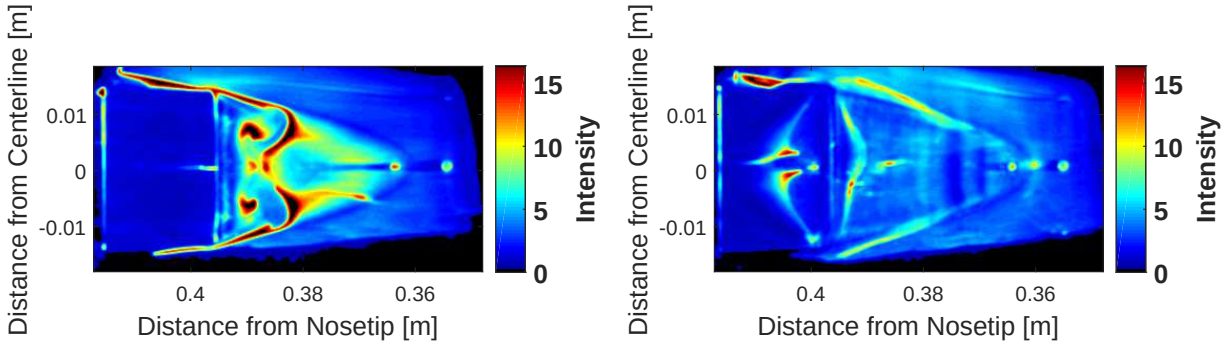

Figure 8. Oil flow on the model with 30° ramp. Left: Re = 11.6×10^6/m in noisy flow. Right: Re = 11.4×10^6/m in noisy flow.

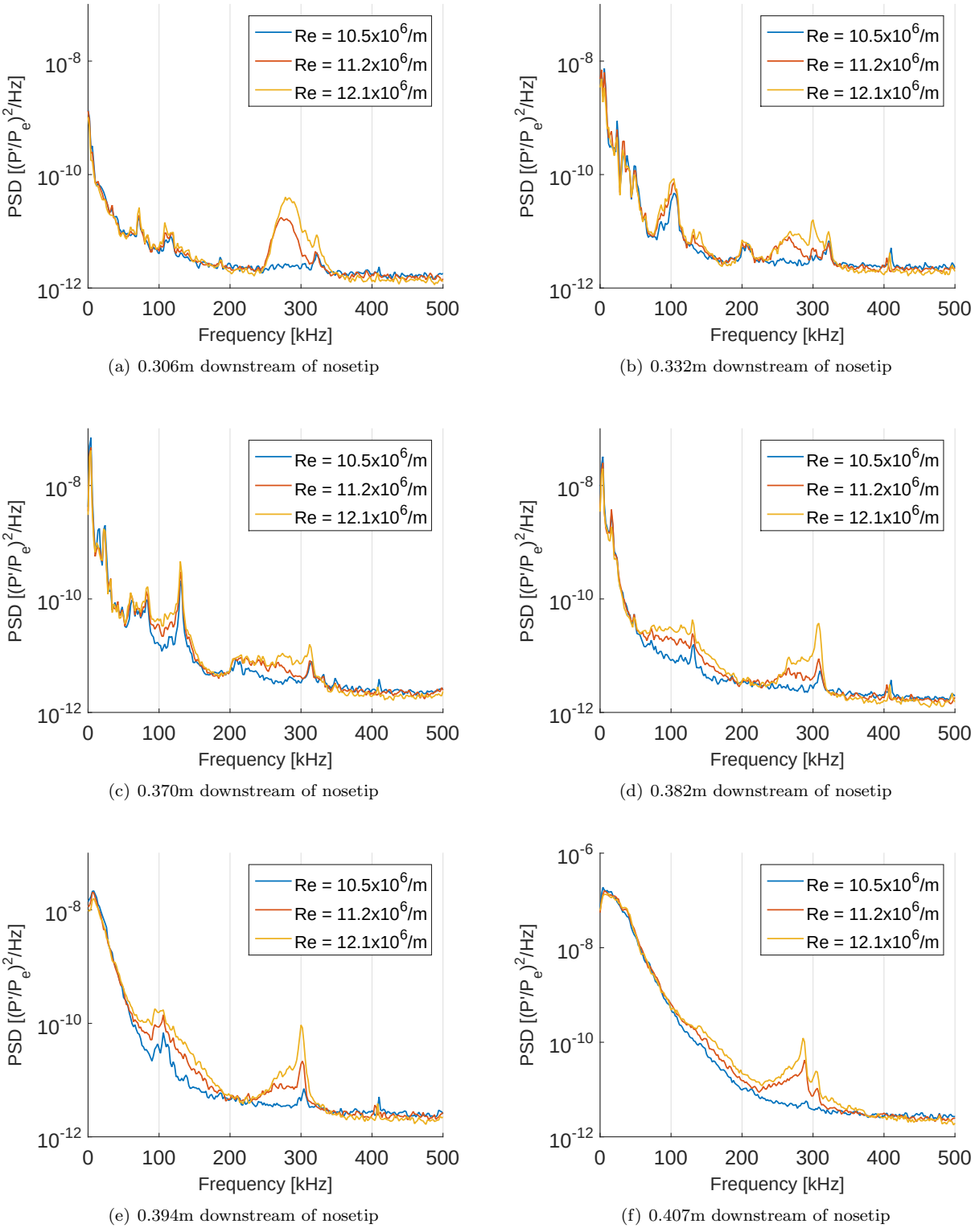

(a) 0.306m downstream of nosetip

(b) 0.332m downstream of nosetip

(c) 0.370m downstream of nosetip

(d) 0.382m downstream of nosetip

(e) 0.394m downstream of nosetip

(f) 0.407m downstream of nosetip

Figure 9. PSD's along the centerline of the model with 20° ramp.

C. Future Work

Future work will focus on developing the capability to image oil flow through the top insert of the BAM6QT. This would allow for the oil to sit on top of the model and improve the quality of the images. Additionally, improvements to the model would allow for surface sensor to be placed closer to the compression corner where the separation is present. An electronic point perturber has also been developed and the introduction of a controlled point disturbance through a compression is possible. Lastly, the use of off-surface measurements will allow for tracking of instabilities through the shear layer off the surface.

IV. Flow Characteristics in the BAM6QT

Characterization of the BAM6QT performance is ongoing and includes the conditions under which quiet flow can be achieved, the noise levels present during a run, and the uniformity of the flow. It is important to understand the limitations of quiet flow in the tunnel so that accurate conclusions can be drawn from measurements. The work presented in this section covers three objectives. First, the temperature distribution along the nozzle wall was varied to explore effects on the maximum quiet pressure. Second, measurements were taken to investigate the source of an increase in tunnel noise occurring approximately two seconds into the run. Finally, attempts were made to measure the pressure fluctuations in the frequency band in which second mode instabilities are typically present.

A. Temperature Distribution on the Nozzle

Wall heating and cooling have been shown to affect the stability of a boundary layer. Demetriades[7] found that local surface heating delayed transition and resulted in a decrease in turbulent bursts. In addition, Masad and Nayfeh[8] calculated the effects of heating strips on boundary-layer stability on a flat plate and found that while uniform heating can destabilize a boundary layer, the opposite result can be achieved with a heated strip. This is assumed to be because the heat transfer reverses direction downstream of the strip, and the fluid is effectively cooled by the wall, thus stabilizing the flow.

Four band heaters were used to vary the temperature along the diverging sections of the nozzle. Temperatures were measured with thermocouples installed at various locations along the outside of the nozzle. Because the upper wall of the nozzle has been found to be consistently hotter than the lower wall, only thermocouples located on the side wall were used. These thermocouples generally measure the average temperature between the upper and lower wall. It should be noted that thermocouples cannot be installed on the inside of the nozzle without disturbing the flow, and the temperature measured on the outside of the nozzle is not the same as it is on the inside. Computations such as those presented by Skoch[9] and Schneider, Rufer, Randall and Skoch[10] are needed to determine how the temperature differs on the inner and outer nozzle wall. The stagnation pressures chosen for these measurements were between 170 psia, which is the maximum quiet pressure, and 185 psia. Any effects on the maximum quiet pressure would be seen in runs with these initial stagnation pressures. In addition, there are a larger number of turbulent bursts at higher pressures. Therefore, the effects on the number of turbulent bursts can be more easily seen at higher pressures.

Because Masad and Nayfeh's work suggested that a decreasing temperature gradient could stabilize the flow, the heaters were set so that there were higher temperatures close to the throat and lower temperatures downstream. The farthest-upstream heater had a maximum set point of 120°C because the highest safe temperature for the nickel nozzle in the BAM6QT is 150°C. The farthest-downstream heater had a maximum set point of 40°C, since the goal was to slowly taper the heating until near room temperature. Figure 10 contains examples of temperature distributions along the nozzle. Axial position, z, is measured in inches downstream of the throat.

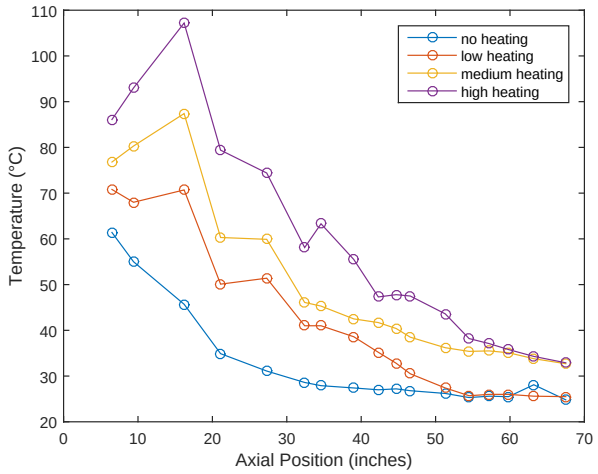

Figure 10. Example temperature distributions along the outside of the nozzle. No insulation was used, and the thermocouples were exposed to the air.

Hot films are installed on the nozzle wall and provide a qualitative measure of the amount of heat transfer during a run. The uncalibrated hot-film signal indicates whether or not the flow is quiet, since turbulence results in much higher heating than laminar flow. Figure 11 shows the hot film trace for a typical run with an initial stagnation pressure, P_{0i}, of 170 psia and no heating. The spikes in the signal indicate turbulent bursts. Quiet flow is almost always achieved by 0.5 seconds, and continues for roughly 4 seconds. However, the turbulent bursts increase in number at approximately $t = 2$ s, as in Figure 11. The increased number of bursts is accompanied by a general increase in noise levels, a topic which is discussed in the following section. As a result of tunnel start-up and this noise increase, data are typically analyzed between $t = 0.5$ s and $t = 2$ s. Therefore, the same time period of $t = 0.5$ s to $t = 2$ s was considered for determining the fraction of time the flow was quiet, for all runs.

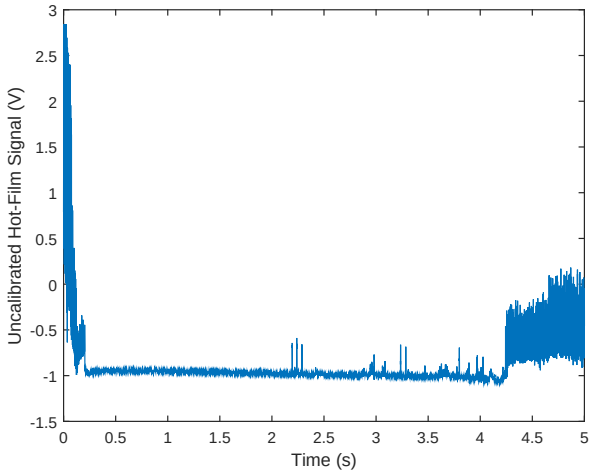

Figure 11. Time trace of the uncalibrated hot film during a run with $P_{0i} = 170$ psia.

In order to determine whether or not the flow was quiet in a time interval, the standard deviation of the hot film values during that interval was computed. The standard deviation for a hot film trace of quiet flow resulting from an initial stagnation pressure of $P_{0i} = 170$ psia is approximately 0.003 V. Since that value decreases for lower stagnation pressures, time periods for which the hot film signal standard deviation was less than or equal to 0.003 V were considered to contain quiet flow.

Figure 12 is a plot of the percentage of time between t = 0.5 and 2 seconds which is quiet versus the maximum temperature measured by the thermocouples for various amounts of heating. Each data point represents a different run. The runs with $P_{0i} = 170$ psia generally contain quiet flow for around 95% of the run between $t = 0.5$ s and $t = 2$ s. This is expected, since that time range was chosen because it contains mostly quiet flow if P_{0i} is less than the maximum quiet pressure of 170 psia. Also as expected, as the initial stagnation pressure increases, the percentage of time which is quiet flow decreases. However, no relationship between the heating and the amount of quiet flow is evident. The scatter for the higher initial stagnation pressures is likely due to inherent randomness, and there is no apparent correlation between temperature distribution and percentage of quiet flow.

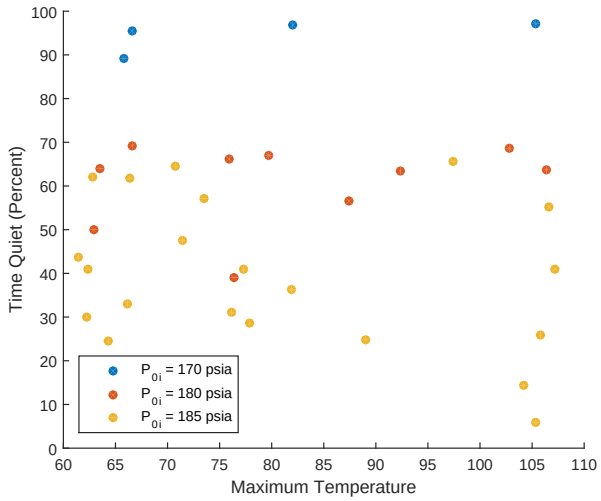

Figure 12. Percentage of run time between $t = 0.5$ s and $t = 2$ s that was quiet verses the maximum measured temperature. Data are shown for all three P_{0i} values.

It is also important to note that even if the initial stagnation pressure was as high as 185 psia, the highest stagnation pressure during the run which exhibited quiet flow was generally still around 170 psia. This can be observed in the signal from the pitot probe with $P_{0i} = 185$ shown in Figure 13. The pitot probe contains a Kulite pressure sensor and was positioned on the centerline at an axial location of $z = 93.6$ in. The combination of the period of noisy flow at the start of the run and the additional turbulent bursts lead to smaller percentages of quiet flow. However, even though the maximum quiet pressure is still 170 psia, a higher initial stagnation pressure yields a higher Reynolds number at the onset of quiet flow for a given stagnation pressure. This is because a higher P_{0i} results in a lower stagnation temperature and thus a higher Reynolds number. Thus, running the tunnel with a higher P_{0i} can give larger Reynolds numbers while still achieving small time periods of quiet flow.

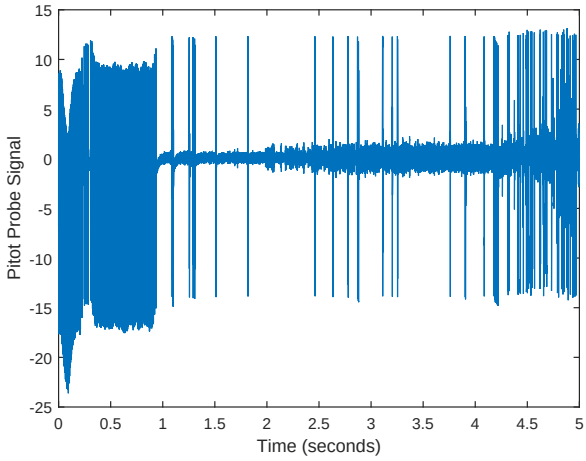

Figure 13. Raw pitot probe signal for a run with $P_{0i} = 185$.

Figure 13 shows that while a run may not contain sufficient time with quiet flow to be considered quiet, there are often time segments of at least 0.1 seconds that do have quiet flow. Generally, this is the length of time used by researchers in the BAM6QT to analyze data, so quiet segments at least that long are useful. Due to the random nature of the turbulent bursts, it is not possible to control exactly which stagnation pressure would exhibit quiet flow. Nevertheless, turbulent bursts appear in the hot-film signal and can be avoided when processing data. Figure 14 shows the hot-film signal plotted with the signal from the the pitot probe. The pitot-probe signal is the raw voltage, which has been scaled down by a factor of 100 and offset by a constant value to allow visual comparison with the hot film signal. All noise that is in the pitot-probe signal also appears in the hot-film trace. Additionally, there is noise picked up by the hot film that is not in the pitot-probe signal. This suggests that the hot film is a sufficient measure of quiet flow, because all times that are quiet according to the hot film are also quiet according to the pitot probe. Thus, when models are used which do not contain a pitot probe, the hot film alone can be trusted to confidently ensure quiet flow in a desired time period. This is useful especially at high P_{0i} where there are many turbulent bursts.

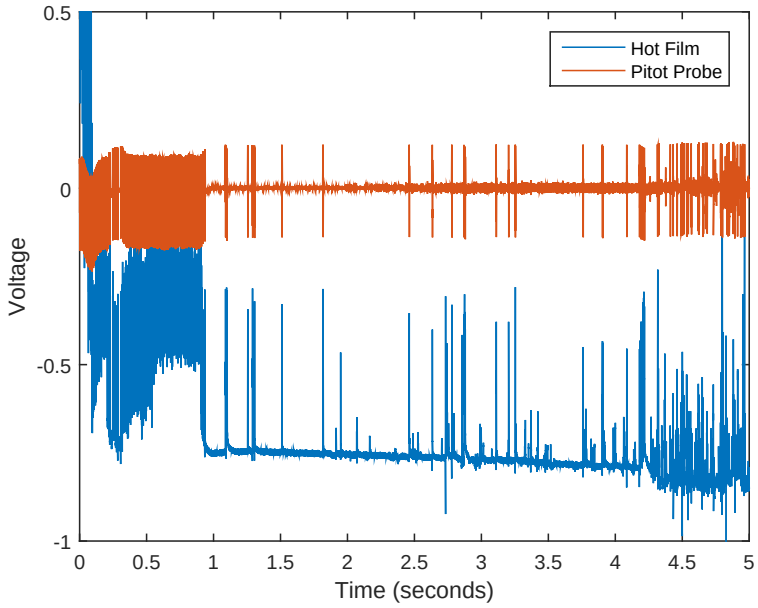

Figure 14. The uncalibrated hot film and pitot-probe signals for a run with $P_{0i} = 185$. Values are qualitative only.

B. Noise Increase

An increase in tunnel noise two seconds into the run was found by Steen.[11] The reason for this increase in disturbances is unknown, although Borg[12] and Casper, Beresh and Schneider[13] discuss a possible source. They suggest that the disturbances are caused by an increase in temperature fluctuations in the contraction after $t = 2$ s. However, this noise increase is still not understood. Steen[11] found that for data taken on the centerline, the noise increase occurred consistently at $z = 93.6$ inches but not at $z = 84.9$ in. Furthermore, her data show a larger increase in noise levels for an initial stagnation pressure of 140 psia than for 90 psia. Measurements presented here include runs with initial stagnation pressures of 90, 130 and 170 psia. The pitot probe was located on the centerline and was moved axially between runs in an attempt to find a more precise location where the noise increase begins.

The noise level of the tunnel is the root-mean-square of the pitot-pressure fluctuations normalized by the mean pressure. It is calculated by integrating and square-rooting the power spectral density of the normalized fluctuations for a duration of 0.1 seconds. The mean pressure is given by the DC signal of the Kulite sensor, and the fluctuations for quiet flow data are taken from the AC signal. Figure 15 contains the noise levels throughout the runs for all three initial stagnation pressures at various axial locations.

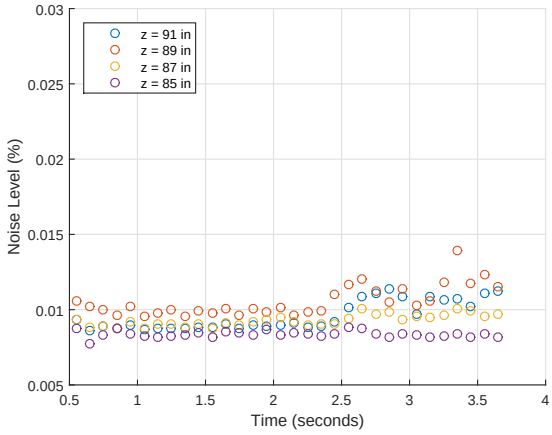

(a) Noise levels calculated from runs with $P_{0i} = 90$ psia.

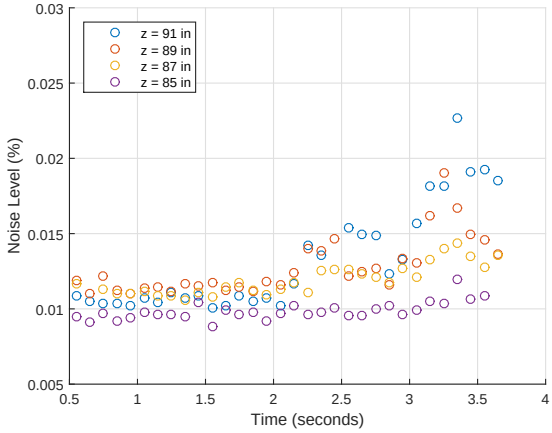

(b) Noise levels calculated from runs with $P_{0i} = 130$ psia.

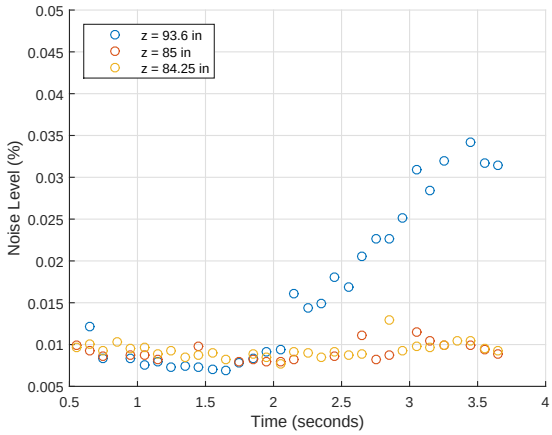

(c) Noise levels calculated from runs with $P_{0i} = 170$ psia.

Figure 15. Noise levels for all three initial stagnation pressures at various axial locations.

There is an increase in the noise level seen in the $P_{0i} = 90$ psia case for locations downstream of $z = 87$ in. The disturbance increase starts at $t = 2.5$ s. For the $P_{0i} = 130$ psia case, the increase happens slightly earlier in the run and is much greater in magnitude. Large increases in noise begin at a similar axial location of $z = 87$ in. The farthest upstream distance tested, $z = 85$ in, also shows a slight increase in noise level by the end of the run, but not nearly to the extent of the $z = 89$ in or $z = 91$ in case. Both the 90 psia and the 130 psia initial stagnation pressure measurements indicate noise levels that are low in upstream positions and, in general, increase downstream. There are only three runs compared for conditions of $P_{0i} = 170$ because the rise in noise level appeared to be visible in the pitot probe signal (plotted in Figure 16) even in the position which was the furthest possible upstream location with the probe used for these runs. The pressure fluctuations increase in number but the magnitude of the fluctuations is small compared to those seen in more downstream locations. Thus, the noise levels plotted in Figure 15(c) do not contain this increase. More data will need to be taken at various axial locations to determine if the increase in noise levels for runs with $P_{0i} = 170$ begin at the same axial location as for the lower P_{0i} cases.

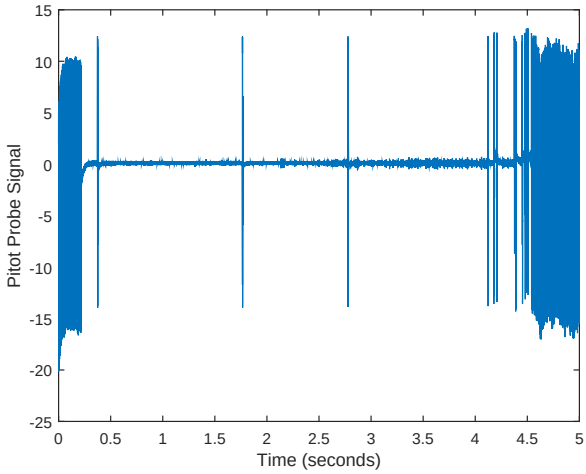

Figure 16. Pitot probe signal during a run with $P_{0i} = 170$, $z = 84.25$.

C. Higher-Frequency Fluctuations

Kulite pressure transducers, which have a resonant frequency around 200 to 350 kHz, are generally used to measure freestream fluctuations. The roll-off frequency of the Kulite is approximately one-fifth of the resonant frequency,[11] and Kulites are typically considered reliable up to 50 kHz. However, the frequencies associated with the second-mode instability on models typically used in the BAM6QT are on the order of 200 to 400 kHz. Measurements were taken with a PCB sensor, which has a resonant frequency greater than 1MHz, to gather information regarding the high-frequency content of freestream noise which is relevant to the second mode. There are difficulties in capturing that portion of tunnel noise. At those higher frequencies, the fluctuations under quiet flow are small compared to the noise floor in the PCB sensor, and often the signal-to-noise ratio is too small to extract any useful data. Figure 17 compares the power spectral densities of two time segments for which Re $= 6.8\times10^6$/m, one under quiet flow and one under noisy flow. Also plotted is the PSD of the pre-run noise. The reason for the peak around 280 kHz is unknown, but it is not a feature of the flow, since the no-flow PSD also contains that peak. While the fluctuations that occur in noisy flow are well above the electronic noise floor of the sensor, the quiet fluctuations are only significantly larger than the sensor noise at low frequencies. As a result, no reliable information can be obtained regarding the quiet flow pressure fluctuations in the desired frequency range of 200 to 400 kHz.

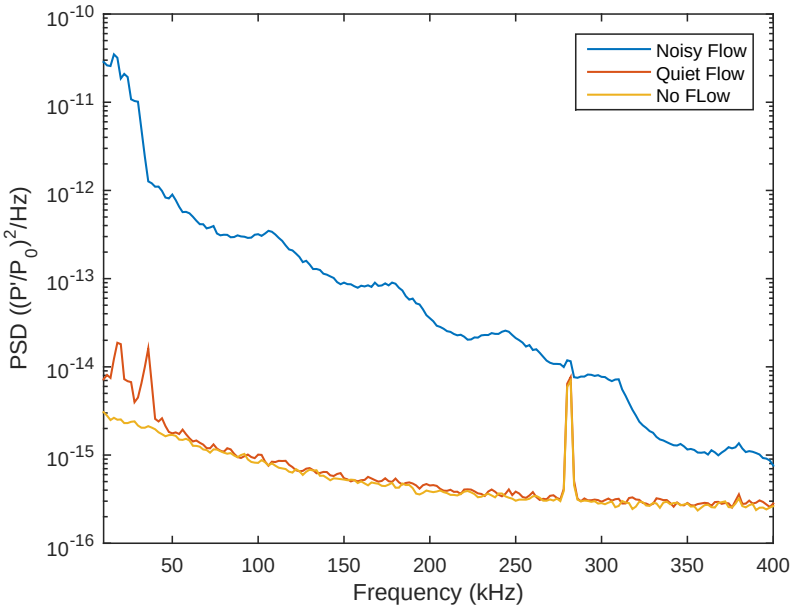

Figure 17. Power Spectral Densities comparing pressure fluctuations for noisy flow, quiet flow and no flow.

V. Design of a Flared Inlet Centerbody using STABL

A. Background

Conventional hypersonic wind tunnels have turbulent boundary layers on the nozzle wall that radiate noise onto the test article. The high levels of noise can have an effect on the transition process as well as altering the pressure fluctuations under a turbulent boundary layer.[14] In order to study transition at freestream noise levels similar to those experienced by actual flight vehicles, it is necessary to perform tests in a quiet wind tunnel. These facilities maintain a laminar boundary layer on the nozzle wall, thus reducing the freestream noise. To maintain a laminar boundary layer, facilities currently use techniques such as a bleed-slot upstream of the throat, highly polished nozzles, and air filters to eliminate small particulates.[15] Additionally, current nozzle designs are elongated in order to reduce the Görtler instability which develops on concave surfaces. In order to develop state-of-the-art hypersonic quiet wind tunnels, new techniques must be developed.

As noted by Schneider, a technique that may aid in the development of higher-Reynolds number quiet tunnel facilities is the use of microperforated walls to perform suction over an area of the nozzle wall. In his review paper on hypersonic quiet tunnels, Schneider also outlines early developments using nozzle suction by Klebanoff, Groth, and Beckwith.[14] Removing mass through the nozzle wall via small perforations can stabilize the boundary-layer profile. If the boundary layer is stabilized, the laminar boundary layer on the nozzle wall will result in quiet-tunnel conditions. Two different problems may arise when using nozzle-wall suction at hypersonic speeds. The first is that the patterning of small perforations may excite the Görtler instability causing transition on the nozzle wall and resulting in a turbulent boundary layer. Second, uniform suction is necessary to maintain axisymmetric flow but can be difficult to achieve. The focus of current research is to perform mean flow and stability computations to develop a geometry with a suction section that can be tested in the Boeing/AFOSR Mach-6 Quiet Tunnel. This is the first step in a risk reduction study towards the development of future quiet wind tunnels.

B. Geometry and Grid Generation

In order to support the nozzle-wall suction development, a geometry must be developed that can be tested in the current facility. The proposed geometry resembles the inlet centerbody of the SR-71 Blackbird with a flared aft-end and will therefore be referred to as a flared inlet centerbody. The geometry has three distinct regions, as shown in Figure 18. The model begins with a 7° half-angle cone to promote the growth of the second-mode instability. Following the cone is a turning region which directs the flow towards the flared aft-body. It is important that the turning region does not cause the flow to separate. The flared aft-body should amplify any Görtler instabilities since it has a concave surface. If this design is constructed for experimental testing, a suction region can be placed in the 7° half-angle cone portion of the model.

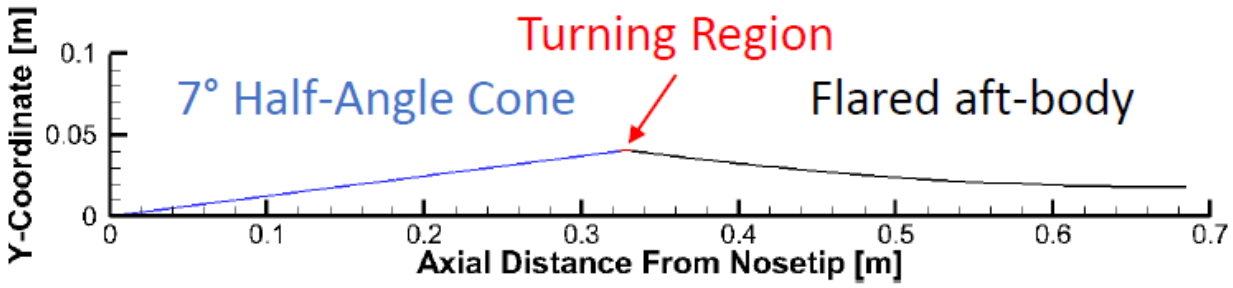

Figure 18. Flared inlet centerbody showing three distinct regions.

The grid generation module for mean flow and stability computations using STABL requires the user to generate the points along the surface of the body. The body points were created using a MATLAB script. The current geometry begins with a hemispherical nose of radius 0.1 mm composed of 10 points. This is

followed by the 7° half-angle cone which contains 438 body points. The 10 points in the turning region create a radius of curvature of 3 cm. The flared-aft body has a radius of curvature of 3 meters and contains 65 points. The total model length is 69 cm. Figure 19 shows the distance between points along the surface of the body. An attempt was made to keep the spacing from the nosetip through the turning region as smooth as possible to reduce computational issues that may arise from large jumps in spacing. Stretching between points is used in the flared aft-body region to reduce the total number of points in the body to save computational time. A detrimental effect of the stretching will be seen when computing the Görtlernumbers on the flared aft-body.

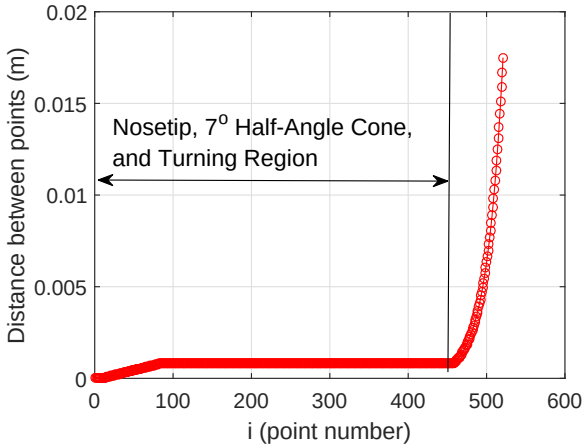

Figure 19. Spacing between points along the surface of the body. Stretching is implemented on the flared aft-body region.

C. Preliminary Results

1. Freestream Conditions for Computations

STABL was used to perform computations on the flared inlet centerbody at a freestream stagnation pressure of 160 psia. This pressure is near the maximum quiet stagnation pressure of the Boeing/AFOSR Mach-6 Quiet Tunnel facility. Table 1 summarizes freestream conditions for the simulation. An isothermal model wall temperature boundary condition of 300 K was used, assuming the model starts near room temperature. When performing mean flow calculations, the flow was set to be axisymmetric. Chemical vibrations were turned off and the STABL "non-reacting air" model was used to reduce the time necessary for stability calculations.

Table 1. Freestream conditions used for STABL computations with flared inlet centerbody geometry.

M_∞	P_0 [psia]	T_0 [K]	T_∞ [K]	ρ_∞ [kg/m^3]	T_{wall} [K]
6.0	160	425	51.9	0.0469	300

2. Mean Flow Analysis

When designing the flared inlet centerbody, one of the most important features is that the turning region does not cause boundary-layer separation. Figure 20(a) is a contour plot of the Mach number distribution. The shock is shown as the solid black line. The Mach number behind the oblique shock that originates near the nosetip is 5.4. As the flow is turned around the expansion corner, the Mach number increases as expected. In order to verify that there is no separation or recirculation region, it is necessary to look at the

velocities of the flow in the streamwise and axial coordinates. Figures 20(b) and 20(c) show the contour plot of u-velocity (streamwise direction) and v-velocity (radial direction) in meters per second. It can be seen that there are no signs of recirculation or flow separation. All values of u are positive and the v components are positive in front of the expansion corner and negative behind the expansion. This verifies that the flow remains attached over the entire length of the model.

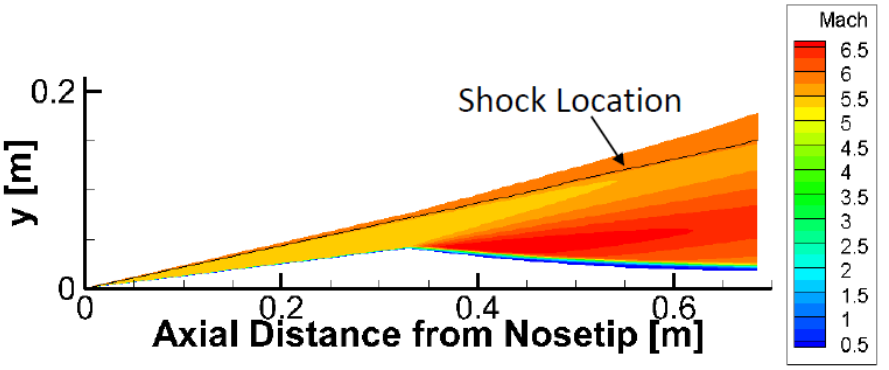

(a) Mach Distribution

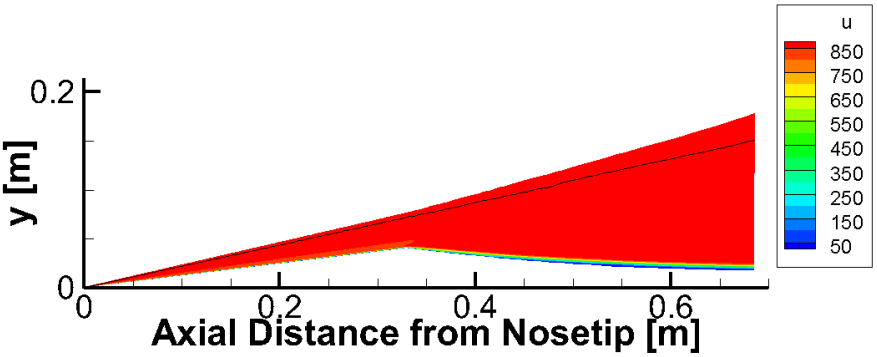

(b) u-velocity in m/s

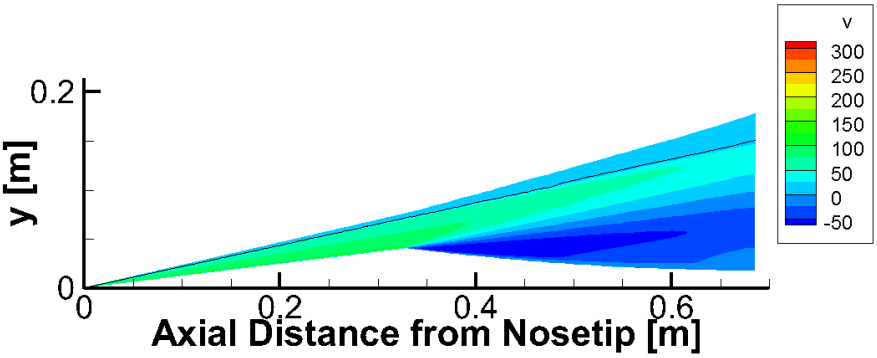

(c) v-velocity in m/s

Figure 20. Contour plots for the mean flow analysis of the Mach number and velocities in the streamwise and radial directions.

The Görtler number (G) is computed on the flared aft-body using $R_\theta(\theta/r)^{1/2}$ where R_θ is the boundary-layer Reynolds number based on the momentum thickness, θ, and r is the radius of curvature. Figure 21 is a plot of the Görtler number versus the distance from the nosetip. It can be seen that G ranges from 2 up to a peak value of 12 near the end of the model. It is clear that the stretching of the grid near in the flared aft-body region causes a loss in resolution for distances greater than 0.5 m from the nosetip. Future calculations will minimize the stretching to increase the resolution near the end of the model at the cost of increased computational time.

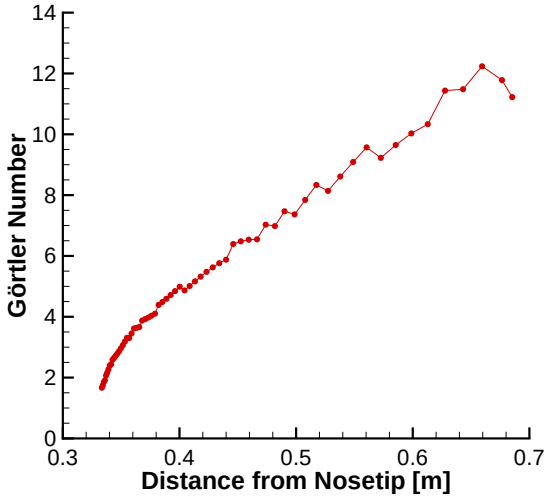

Figure 21. Görtler number computed using the mean flow solution for the flared aft-body.

3. Stability Analysis

The PSE-Chem module in STABL is suited for computing both the first- and second-mode instabilities. For sharp cones at 0° angle of attack at Mach 6, the instability with the highest amplification rates was computed by Mack to be a two-dimensional second-mode wave.[16] The second-mode frequency is inversely related to the boundary-layer thickness. It can be estimated using $f = v_e/2\delta$ where f is the second-mode frequency, v_e is the edge velocity, and δ is the boundary-layer thickness. The boundary-layer thickness, computed using the maximum enthalpy criterion, and the estimated second-mode frequency are shown in Figure 22. Over the 7° half-angle cone portion from the nosetip to 0.32 m, the boundary layer is relatively thin and second-mode frequencies are estimated to be above 400 kHz. After the turning region, the boundary-layer grows by a factor of six and second-mode frequencies are estimated to be below 200 kHz.

A stability analysis was performed over an area that covered distances from 0.05 m to the end of the model using 150 evenly spaced points. Frequencies between 5 kHz and 600 kHz were included and also contained 150 evenly spaced points. This region was chosen to best analyze the flow from near the end of the 7° half-angle cone region to the end of the model. Performing stability computations near the nosetip and at higher frequencies would have greatly increased the required computational time. Figure 23 shows the stability diagram with the computed amplification rates. Over the 7° half-angle portion, high-frequency instabilities dominate with amplification rates near 60. As the flow is turned, all frequencies are attenuated. Starting approximately 0.4 m from the nosetip on the flared aft-body, a low frequency second-mode instability develops but with amplification rates four times lower than those calculated on the 7° half-angle cone.

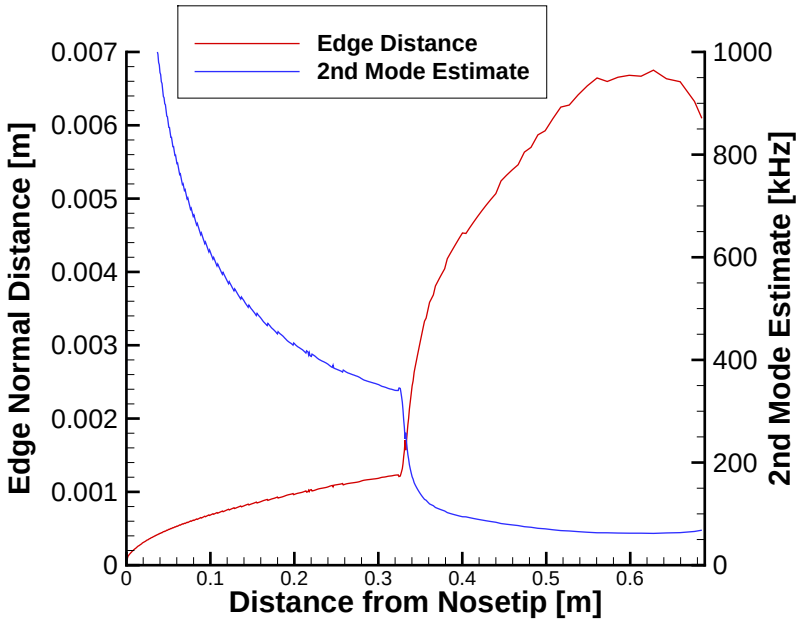

Figure 22. Edge normal distance computed using the peak enthalpy criterion along with the second-mode frequency estimate.

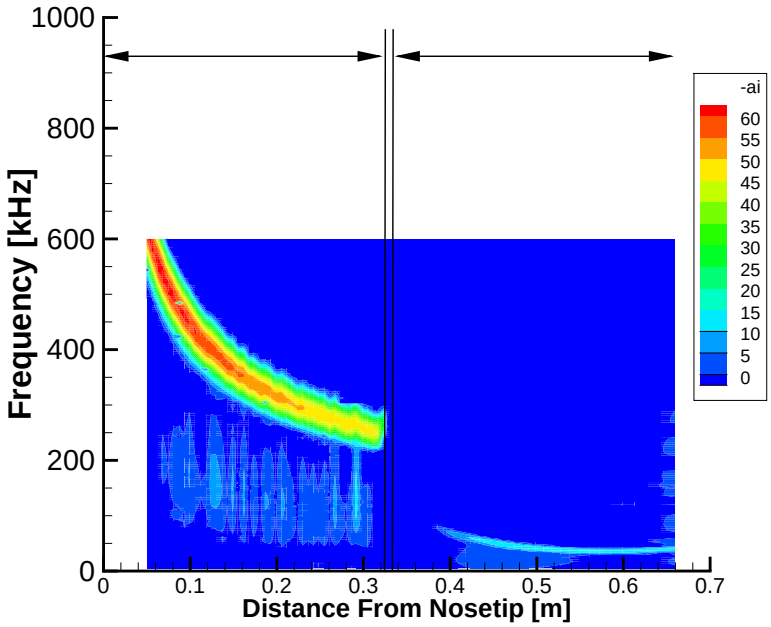

Figure 23. Stability diagram with amplification rates over the area covered by x = 0.05 m to the end of the model and frequencies from 5 kHz to 600 kHz.

N factors for many frequencies are plotted in Figure 24. Three frequencies of interest are highlighted with thicker lines. Over the 7° half-angle cone portion of the model, the frequency that reaches the highest N factor is 280 kHz (thick black line). The N factor of almost all frequencies decreases as the flow is turned beginning at 0.32 m form the nosetip with one exception. A frequency near 9 kHz (thick green line) appears to undergo explosive growth reaching N factors of over 60 at the aft end of the model. The validity of this result needs to be further studied since Figure 23 does not indicate that a low frequency instability should experience such significant growth. In the flared aft-body region, a frequency of 36.95 kHz reaches a maximum N factor of about 4. Based on these results, if a model is fabricated it is suggested that PCB132 fast pressure sensors be used on the 7° half-angle cone portion while Kulite XCQ-062 sensors be used to measure the low-frequency pressure fluctuations on the flared aft-body.

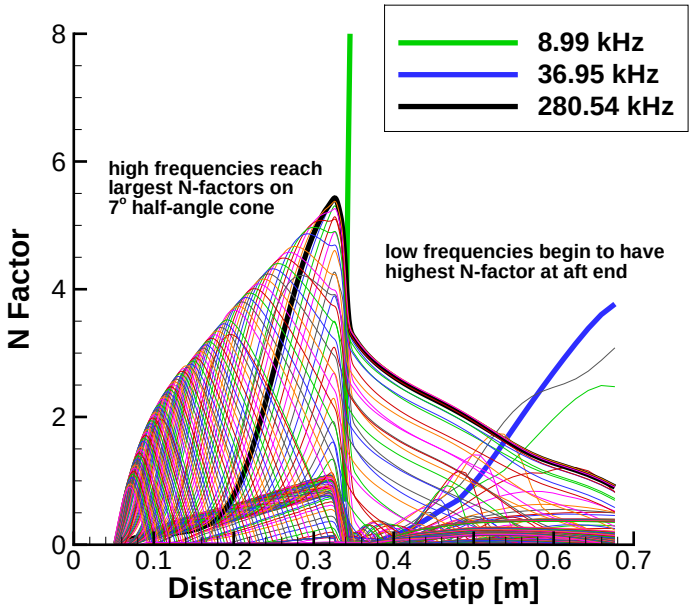

Figure 24. Computed N factors for stability analysis beginning at x = 0.05 m.

D. Ongoing and Future Computations

Two different parametric investigations are currently being conducted. The first is changing the turning region curvature to see the effect on the flow over the flared aft-body. Radii of 0.03, 0.3, and 3.0 meters are being tested. Josh Edelman is performing computations to determine any effects of changing the radius of curvature of the flared aft-body. The results from these computations will be used to determine the final geometry that will be fabricated for experiments.

VI. Purdue 3 Inch Shock Tube

A. Background

The Purdue 3 inch shock tube is intended for calibrating PCB sensors by producing low amplitude shocks. A shock wave is generated by bringing the driver and driven sides of the tube to desired run conditions and then bursting the separating diaphragm. Diaphragm material is typically Mylar plastic and is burst by discharging a capacitor through Nichrome wires, which contacting the diaphragm, vaporizing the wires and causing a shock wave. Pressures are controlled before the shock and data during the shock is obtained from PCB and Kulite sensors with oscilloscopes.

PCB sensors are commonly used in the BAM6QT to precisely measure pressure fluctuations, and so an accurate calibration is necessary. The manufacturer only performs a rudimentary calibration which can differ from a robust calibration by as much as 18%.[17] Calibration using the Purdue 3 inch shock tube was effectively demonstrated by Berridge,[17] and will be continued with this work.

B. Improvements To the Purdue 3 Inch Shock Tube

In the previous iteration of the shock tube, a typical procedure for producing a shock included controlling pressures by hand, manually setting oscilloscopes for data collection, closing the connecting valves, and then bursting the diaphragm. In this configuration, low pressures were difficult to maintain due to leaks significantly increasing the pressure when the valve closes. Additionally, since the pre-shock pressures were read while the operator was bursting the diaphragm, accurate pressure recordings were difficult to obtain.

Improvements have been made to the shock tube system including accurate static pressure measurement and recording before the shock, simplification of apparatus for ease of use, and increased repeatability. To address these issues, a LabVIEW program was designed to perform the majority of operation from a single workstation. An automated valve, high accuracy sensors, and a data acquisition unit were also implemented to interface with this program and improve operation. With the current configuration, driven pressures can be set and maintained automatically, pressures monitored and recorded, oscilloscopes set up for data acquisition, and the burst system operated from a single computer. The final configuration will utilize two automated butterfly valves to control pressures in both the driver and driven sections, but the current configuration, as seen in figure 25, only has a single valve. Because of this, the two sections are depressurized together to the driver pressure, the vacuum line connecting the two sections is closed, and the driven section is depressurized separately. This works reasonably well since leakage across the diaphragm is limited, and so the pressure on the driver side stays roughly constant for short periods of time. Pressure is controlled on the driven side with the automated valve, and is recorded for both driver and driven sections when the burst command is executed, giving an accurate measurement immediately before the shock is created.

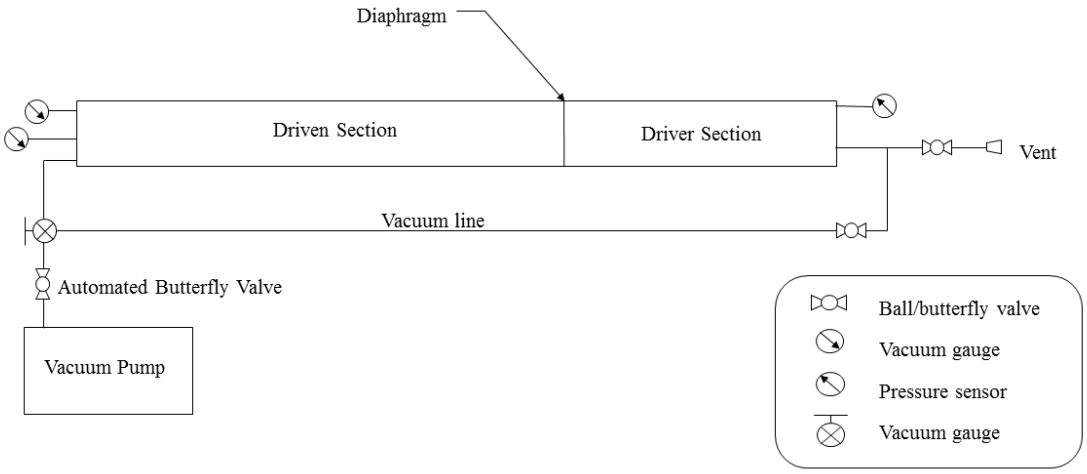

Figure 25. Purdue 3 inch shock tube air system schematic.

C. Pressure Control With VAT Butterfly Valve

To control pressures, a PI controller in the automated butterfly valve was tuned. Since the driver section must be depressurized while connected to the driven side, its response is substantially different from the driven section alone. Because of this, two different sets of gains were used for pressure control. Typical behavior for driven section pressure response and combined section pressure response is shown in figures 26 and 27, respectively. While it can take more than 2 minutes to reach the commanded pressure, control is successful in both configurations to within a low margin of error. Control of the driver section will also be dramatically improved with the addition of the second automated butterfly valve, allowing for complete pressure control of the driver section. The second valve will also eliminate the need to include the vacuum line in the pressure control system, likely reducing the settling time.

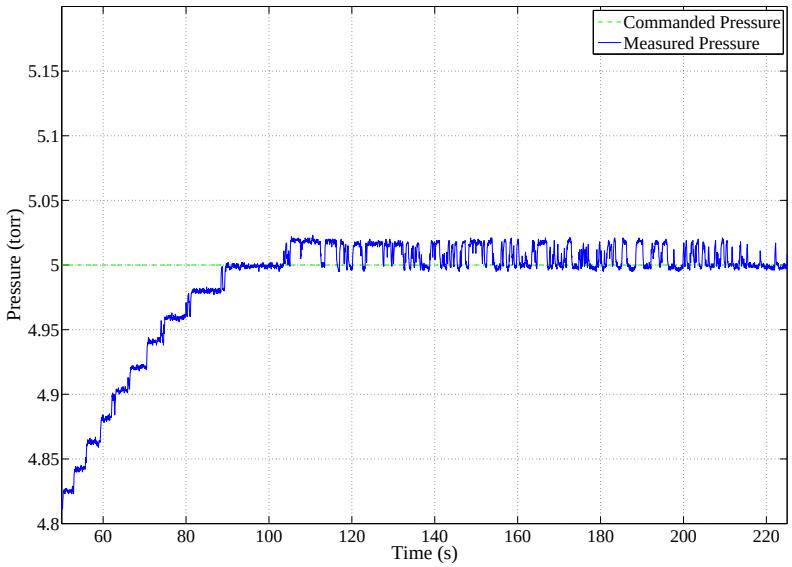

Figure 26. Driven section pressure control for 5 Torr command.

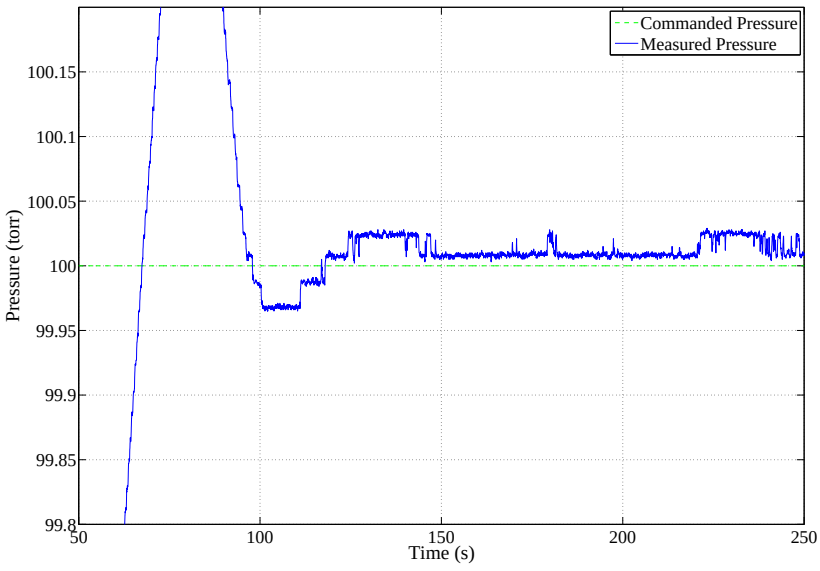

Figure 27. Driver and driven section pressure control for 100 Torr command.

VII. Conclusion

1. Infrared images were taken on a 7° half-angle cone at a 6° angle of attack. The distortion from the wide-angle lens used was corrected, and the temperature difference between an image during a run and a pre-run image was presented. Several streaks are obvious and indications of transition can be observed. Comparisons were made between temperature changes measured by the IR system with those measured with TSP. The noise level is lower for the IR measurements than for the TSP measurements, and streak location and amplitude were repeatable.

2. Experiments were completed in order to determine the flow over an inherently three-dimensional model of a cone with a slice and ramp. Oil flow and surface pressure sensor measurements were presented in order to provide picture of the surface flow behavior. Through the expansion from the straight cone to the slice, the second-mode instability was damped. Lower frequency instabilities developed along the flat portion of the model and continued onto the ramp surface. In this region, the oil flow showed accumulations of oil on the slice but closer to the ramp corner than any sensors on the slice. Due to the lower-speed flow in a separation, it is thought that the surface pressure fluctuation amplitudes would be greater in this region. However, this was not seen in the current measurements. More precise measurements and further work is needed to characterize the flow and transition. Additionally, off-surface measurements will be conducted in the future.

3. Changing the temperature distribution along the nozzle proved to be ineffective in increasing the maximum quiet pressure. However, the hot film time trace can be used to ensure that the time period of interest contains quiet flow. Quiet portions of runs with initial stagnation pressures greater than 170 psia can then be used, which increases the maximum quiet Reynolds number. The magnitude of the noise increase two seconds into tunnel runs depends on the initial stagnation pressure and the axial location of the pitot probe used to measure the pressure fluctuations. Lower-pressure runs contained smaller noise increases which began slightly later in the run than those with higher pressures. Finally, attempts to measure the high-frequency content of tunnel noise were ineffective. The noise floor of the PCB sensor prohibited any reliable signal for frequencies above 50 kHz under quiet flow.

4. Initial designs for a flared inlet centerbody show that the flow can be turned without boundary-layer separation. High-frequency second-mode waves grow on the 7° half-angle cone portion of the model reaching N factors of approximately 5.8. On the flared aft-body, Görtler numbers between 2 and 12 were computed. This number indicates that the flared region will be susceptible to the Görtler instability. More refined computational techniques and experiments are needed to determine the extent to which microperforations on the cone affect the flow in the flared aft-body region.

5. The Purdue 3 inch shock tube has been improved with high accuracy pressure sensors and an automated valve. Automated pressure control has successfully been demonstrated for the shock tube. These improvements will improve the PCB calibration process, making it quicker and more reliable.

VIII. Acknowledgments

Much of this research is funded by the Air Force Office of Scientific Research under grant number FA9550-12-1-0167. Joshua Edelman and Brandon Chynoweth would like to thank the Air Force Office of Scientific Research for funding through the National Defense Science & Engineering Graduate Fellowship (NDSEG) Program. The authors would also like to thank Dr. Tom Juliano and Harrison Yates of Notre Dame University and Dr. Matthew Borg of AFRL for their help in setting up the IR imaging system.

References

[1]Edelman, J., *Secondary Instabilities of Hypersonic Stationary Crossflow Waves*, Master's thesis, Purdue University, School of Aeronautics and Astronautics, December 2016.

[2]Borg, M. and Kimmel, R., "Simultaneous Infrared and Pressure Measurements of Crossflow Instability Modes for HIFiRE-5," *AIAA Paper 2016-0354*, January 2016.

[3]Li, F., Choudhari, M., Chang, C.-L., and White, J., "Analysis of Instabilities in Non-Axisymmetric Hypersonic Boundary Layers over Cones," *AIAA Paper 2010-4643*, June 2010.

[4]Edelman, J., Chynoweth, B., McKiernan, G., Sweeney, C., and Schneider, S., "Instability Measurements in the Boeing/AFOSR Mach-6 Quiet Tunnel," *AIAA Paper 2016-03343*, June 2016.

[5]Babinsky, H. and Harvey, J. K., "Shock Wave-Boundary-Layer Interactions," Cambridge University Press, 2014.

[6]Oberkampf, W. L., Aeschliman, D. P., Tate, R. E., and Henling, J. F., "Experimental Aerodynamics Research on a Hypersonic Vehicle," Sandia Report SAND92-1411, 1993.

[7]Demetriades, A., "Stabilization of a nozzle boundary layer by local surface heating," *AIAA journal*, Vol. 34, No. 12, 1996, pp. 2490–2495.

[8]Masad, J. and Nayfeh, A., "Laminar flow control of subsonic boundary layers by suction and heat-transfer strips," *Physics of Fluids A: Fluid Dynamics (1989-1993)*, Vol. 4, No. 6, 1992, pp. 1259–1272.

[9]Skoch, C. R., *Final Assembly and Initial Testing of the Purdue Mach-6 Quiet-Flow Ludwieg Tube*, Master's thesis, Purdue University, West Lafayette, Indiana, August 2001.

[10]S.P. Schneider, S. J. Rufer, L. R. and Skoch, C., "Shakedown of the Purdue Mach-6 Quiet-Flow Ludwieg Tube," *AIAA Paper 2001-0457*, Januaury 2001.

[11]Steen, L. E., *Characterization and Development of Nozzles for a Hypersonic Quiet Wind Tunnel*, Master's thesis, Purdue University, West Lafayette, Indiana, 2010.

[12]Borg, M. P., *Characteristics of the Contraction of the Boeing/AFOSR Mach-6 Quiet Tunnel*, Master's thesis, Purdue University, West Lafayette, Indiana, 2005.

[13]Casper, K. M., Beresh, S. J., and Schneider, S. P., "Pressure fluctuations beneath turbulent spots and instability wave packets in a hypersonic boundary layer," *AIAA Paper 2011-372*, January 2011.

[14]Schneider, S. P., "Development of Hypersonic Quiet Tunnels," *Journal of Spacecraft and Rockets*, Vol. 45, No. 4, July–August 2008.

[15]Chynoweth, B., Ward, C., Henderson, R., Moraru, C., Greenwood, R., Abney, A., and Schneider, S., "Transition and Instability Measurements in a Mach 6 Hypersonic Quiet Wind Tunnel," *AIAA Paper 2014-0074*, January 2014.

[16]Mack, L. M., "On the Application of Linear Stability Theory to the Problem of Supersonic Boundary-Layer Transition," *AIAA Paper 1974-0134*, January 1974.

[17]Berridge, D. C., *Generating Low-Pressure Shock Waves for Calibrating High-Frequency Pressure Sensors*, Ph.D. thesis, Purdue University, West Lafayette, IN, December 2015.